

**EQUIVALENT CIRCUIT MODEL OF A  
PYROELECTROCHEMICAL CELL**

by  
Josh Augenstein

A thesis submitted to the faculty of  
The University of Utah  
in partial fulfillment of the requirements for the degree of

Master of Science

Department of Mechanical Engineering  
The University of Utah

May 2025

Copyright © Josh Augenstein 2025

All Rights Reserved

The University of Utah Graduate School

STATEMENT OF THESIS APPROVAL

The thesis of Josh Augenstein  
has been approved by the following supervisory committee members:

Roseanne Warren , Chair(s) DD MMM 2025  
Date Approved

Shad Roundy , Member DD MMM 2025  
Date Approved

Himanshu Sant , Member DD MMM 2025  
Date Approved

by Bruce Gale , Chair/Dean of  
the Department/College/School of Mechanical Engineering  
and by Darryl P. Butt , Dean of The Graduate School.

## ABSTRACT

A pyroelectrochemical cell (PEC) is a “self-charging” power cell that uses a porous, pyroelectric material as the separator of an electrochemical double layer capacitor (EDLC). To-date, the fundamental physics of the PEC has been demonstrated through experiment and finite element simulation, however no investigation of cell design and/or operational parameters has been done. This work proposes an equivalent circuit model of the PEC that supports rapid investigation of the coupled design-and-operation space of this joint energy harvesting and storage device. The model is validated against experimental open circuit potential measurements with good agreement. Circuit model elements for equivalent series resistance and pyroelectric current source are directly related to cell design parameters including separator thickness, porosity, and material properties, and electrolyte conductivity. An investigation into the effects of these variables on PEC energy density reveals the importance of minimizing separator porosity, as well as minimum values of pyroelectric coefficient and electrolyte conductivity necessary to meet Internet of Things (IoT) benchmarks. The circuit model’s low-frequency RC time constant, representing charge redistribution and double layer capacitance of small pores, has a significant impact on PEC energy storage, with optimum values determined by the thermal cycling rate of the cell. Overall, this work demonstrates an effective means of designing PEC devices for a wide variety of IoT applications.

For my parents, Susie and Paul.

# CONTENTS

<b>ABSTRACT</b> .....	<b>iii</b>
<b>LIST OF FIGURES</b> .....	<b>vi</b>
<b>LIST OF TABLES</b> .....	<b>viii</b>
<b>NOTATION AND SYMBOLS</b> .....	<b>ix</b>
<b>ACKNOWLEDGEMENTS</b> .....	<b>x</b>
<b>CHAPTERS</b>	
<b>1. INTRODUCTION</b> .....	<b>1</b>
<b>2. MODEL</b> .....	<b>4</b>
2.1 The Equivalent Circuit .....	4
2.2 Theory .....	6
<b>3. PARAMETER EXTRACTION</b> .....	<b>11</b>
<b>4. MODEL VALIDATION</b> .....	<b>14</b>
<b>5. MODEL-BASED PERFORMANCE EXPLORATION</b> .....	<b>18</b>
5.1 Cell Design Parameters .....	19
5.2 Thermal charging rate .....	23
5.3 A Note on Temperature Difference .....	23
<b>6. CONCLUSION</b> .....	<b>26</b>
<b>APPENDICES</b>	
<b>A. SUPPLEMENTARY INFORMATION</b> .....	<b>28</b>
<b>REFERENCES</b> .....	<b>31</b>

## LIST OF FIGURES

1.1	<p>PEC overview. a) Conceptual illustration of a pyroelectric material. A change in temperature with time, <math>dT/dt</math>, induces an electric field, <math>E</math>, in the material due to changes in dipole alignment and the generation of surface charges. b, c) PEC in its resting state showing the full cell schematic (b) and close-up view of EDLC pores (c). d, e) A change in dipole alignment and the generation of an electric field within the separator (d) induces ion movement within the cell, charging the EDLC (e). Diffuse layer ions are not shown in (c, e) for simplicity. f) “Real-world” applications of the PEC experiencing <math>dT/dt</math> include vehicle sensing, flight monitoring, and agricultural sensing. . . . .</p>	2
2.1	<p>a) Equivalent circuit model of the PEC based on a modified Randle’s circuit (<math>R_s</math>, <math>R_1</math>, <math>R_2</math>, <math>CPE_1</math>, and <math>CPE_2</math>) and a pyroelectric current source (<math>I_p</math>). b) Physical representation of how the circuit fits into the cell as well as the cell’s geometric configuration (<math>L_s</math>, <math>L_e</math>, and <math>A_s</math>). c) The conduction (<math>J_c</math>) and displacement (<math>J_d</math>) current densities caused by the pyroelectric electric field (<math>E</math>) moves ions through pores in the separator. d) The ions are stored in the double layer at the electrode-electrolyte interfaces with a Debye screening length of <math>d</math>. . . . .</p>	5
2.2	<p>A simplified illustration of ions passing through a a) micropore versus a b) nanopore and how the screening affects ion movement through the pore. The farther from the pore wall, the lower the electric field becomes and the less influence it has on ion movement. . . . .</p>	10
3.1	<p>Equivalent circuit model best fit with experimental PEC. a) EIS fit at 20°C and 50°C. b) CV fit at 20°C and 50°C. c) Amperometry fit for a 20-50-20°C temperature cycle. Experimental results adapted from [21]. . . . .</p>	12
4.1	<p>Model validation: a) A comparison of experimental, COMSOL Multiphysics simulation, and equivalent circuit model <math>\Delta OCP</math> for a 20-30-20°C thermal cycle repeated four times. b) Single-cycle comparison of part (a) results with associated temperature profiles. c) Equivalent circuit model <math>\Delta OCP</math> predictions for the same <math>\Delta T</math> (20-30-20°C) but different <math>dT/dt</math> rates. The “1x” rate corresponds to the results shown in (a) and (b). d) Equivalent circuit model <math>\Delta OCP</math> predictions for the same <math>dT/dt</math> rate but different <math>\Delta T</math> values. . . . .</p>	17
5.1	<p>Parameter exploration. a) 2D surface plot illustrating the effects of <math>L_s</math> and <math>\sigma</math> on PEC energy density. b) 2D surface plot of <math>p</math> vs. <math>\epsilon_s</math> effects on PEC energy density. c) Increase in PEC energy density with decreasing <math>\gamma_s</math>. d) Effect sizes of the design variables explored in Table 2. Dashed line: low-power IoT application benchmark. . . . .</p>	22

5.2	Low-frequency RC simulations for a 40 min thermal cycle length. a) Effect of $\tau_2$ on cell energy density. A maximum value of $U_A$ is reached at a $\tau_2$ of 205 min. b) Low-frequency RC branch parameters and their effect on $U_A$ for a 40 min thermal cycle. ....	24
S1	Effect of starting OCP on PEC thermal charging. Simulations were conducted with three values of starting OCP (0 mV, 1 mV, and 2 mV) with $R_2 = 950 \Omega$ (a) and $R_2 = 1 \text{ G}\Omega$ (b). ....	29
S2	OCP simulation for one thermal cycle (20-30-20 °C) with $p = 59 \mu\text{C}/\text{m}^2\text{K}$ ("1x pyro coefficient") and $p = 118 \mu\text{C}/\text{m}^2\text{K}$ ("2x pyro coefficient"). ....	30

**LIST OF TABLES**

- 3.1 List of circuit elements and their values at 20°C and 50°C. . . . . 13
- 3.2 List of parameters, extracted values, and affected equivalent circuit elements. . 13
- 5.1 Parameter exploration. . . . . 18
- 5.2 A comparison of known pyroelectric materials and their calculated energy densities within the equivalent circuit model. Pyroelectric coefficients and permittivities were supplied by [7, 21]. . . . . 21
- 5.3 Optimum values of  $\tau_2$  and  $R_2$  (with corresponding  $U_A$ ) for varying thermal cycle lengths. . . . . 24

## NOTATION AND SYMBOLS

---

$dT/dt$	temporal time gradient
$E$	electric field
$\Delta T$	temperature change
$I_p$	pyroelectric current
$R_s$	series resistance
$R_1$	high-frequency resistance
$CPE_1$	high-frequency double layer constant phase element
$R_2$	low-frequency resistance
$CPE_2$	high-frequency double layer constant phase element
$Q$	capacitive value of a CPE
$\alpha$	ideality of a CPE
$L_s$	separator thickness
$L_e$	electrode thickness
$\sigma$	conductivity
$A_{e,act}$	electrode active surface area
$A_s$	separator surface area
$R_g$	universal gas constant
$T$	absolute temperature
$n$	number of electrons transferred
$F$	Faraday's constant
$i_0$	exchange current density
$\epsilon_e$	electrolyte permittivity
$d$	debye screening length
$k_b$	Boltzmann constant
$e$	elementary charge
$N_A$	Avogadro's number
$I$	ionic strength
$J_c$	conduction current density
$J_d$	displacement current density
$\gamma_s$	separator porosity
$p$	pyroelectric coefficient
$\epsilon_s$	separator permittivity
$dD$	electrical displacement
$k$	geometric fitting factor
$U_A$	areal energy density
$Z$	impedance
$\tau_1$	high-frequency time constant
$\tau_2$	low-frequency time constant

---

## ACKNOWLEDGEMENTS

I would like to express my deepest gratitude to my advisor, Dr. Roseanne Warren, for her invaluable guidance, support, and mentorship throughout my research journey. I am equally grateful to my co-advisor, Dr. Shad Roundy, for his constant insight and encouragement. I would also like to thank the third member of my advisory committee, Dr. Himanshu Sant, for his time, feedback, and advice.

Thank you to my fellow lab members in both the Advanced Energy Innovations Lab and the Integrated Self-Powered Sensing Lab for their collaborative spirit, technical assistance, and moral support. In particular, I would like to thank Dr. Tim Kowalchik, whose experimental work provided the foundation for the first pyroelectrochemical cell, forming the basis for my modeling efforts.

Finally, I would like to extend my heartfelt appreciation to my family and friends, whose unwavering support, patience, and encouragement have carried me through to the completion of this thesis and continuously pushed me to reach above and beyond.

# CHAPTER 1

## INTRODUCTION

The rapid expansion of the Internet of Things (IoT) has created a critical need for sustainable, autonomous, low-power sensing devices, particularly in environments without reliable access to conventional power grids. IoT devices often rely on ambient energy sources such as solar, thermal, or kinetic energy to achieve autonomy [12, 29, 30]. However, existing energy harvesting technologies face significant limitations including limited efficiency, high system complexity, reliance on auxiliary energy storage, and sensitivity to environmental conditions [28, 40]. These challenges highlight the necessity for alternative approaches capable of consistently providing reliable power for self-sustaining IoT systems.

A pyroelectrochemical cell (PEC) is a novel device concept for self-charging IoT devices that directly converts ambient thermal energy to stored electrochemical energy [21]. The PEC uses a porous, pyroelectric material as the separator of an electrochemical cell. A pyroelectric material harvests thermal energy in the form of a temperature change with time ( $dT/dt$ ). Temporal temperature gradients produce changes in the polarization of a pyroelectric that induce an electric field within the material (Figure 1.1a). When integrated into an electrochemical cell, the electric field of the pyroelectric separator drives ion movement from one electrode to the other, charging the cell in open circuit condition. Figure 1.1b-e illustrates a PEC with a porous pyroelectric separator integrated into an electrochemical double layer capacitor (EDLC). In its resting state, the PEC stabilizes with an initial ion distribution and a negligible electric field ( $E = 0$ ) (Figure 1.1b, c). Upon heating, the pyroelectric field drives cations and anions toward their respective electrodes, increasing charge density in the electric double layers at the electrode-electrolyte interface (Figure 1.1d, e). In our previous work, we validated the fundamental physics of the PEC and showed that repeated application of a thermal cycle can produce a net increase in

open circuit potential (OCP) [21]. We demonstrated that changes in thermal cycling rate ( $dT/dt$ ) and temperature range ( $\Delta T$ ) produce different outcomes in OCP, as predicted by the constitutive equations of pyroelectricity.

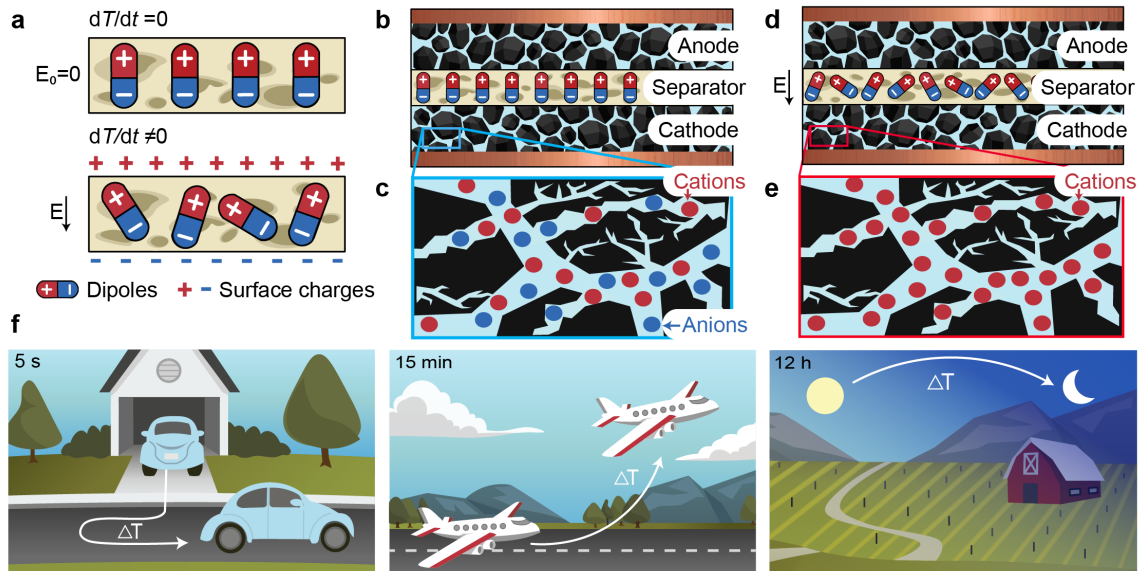


**Figure 1.1.** PEC overview. a) Conceptual illustration of a pyroelectric material. A change in temperature with time,  $dT/dt$ , induces an electric field,  $E$ , in the material due to changes in dipole alignment and the generation of surface charges. b, c) PEC in its resting state showing the full cell schematic (b) and close-up view of EDLC pores (c). d, e) A change in dipole alignment and the generation of an electric field within the separator (d) induces ion movement within the cell, charging the EDLC (e). Diffuse layer ions are not shown in (c, e) for simplicity. f) “Real-world” applications of the PEC experiencing  $dT/dt$  include vehicle sensing, flight monitoring, and agricultural sensing.

Despite demonstrating conceptual feasibility, the current PEC prototype has yet to undergo formal optimization to achieve practical performance levels required for real-world IoT applications. Typical IoT devices require between 50 and 500  $\mu J$  per measurement and data transmission event [4, 6, 41]. Current experimental PEC performance remains below practical benchmarks, achieving only 2.51  $\mu J/cm^2$  (20–30–20) and 12.3  $\mu J/cm^2$  (20–50–20), far from the IoT energy benchmark of 100  $\mu J/cm^2$  [21]. Consequently, further exploration is essential for bridging the gap between existing capabilities and practical energy demands.

The objective of this thesis is to use lumped parameter-based modeling to explore the coupled design and application space of the PEC. In our previous work, we used

a porous polyvinylidene difluoride-barium titanate (PVDF-BT) separator and activated carbon electrodes to fabricate a demonstration PEC device [21]. The device was tested over three different temperature cycles (20-30-20°C, 20-50-20°C, 20-10-20°C), and a COMSOL Multiphysics simulation used to verify the fundamental physics of the device. In practice, a wide range of PEC designs may be achieved by varying, *e.g.* pyroelectric separator material, thickness, and porosity; electrode capacity; and electrolyte conductivity. Likewise, the range of possible “real-world” thermal charging scenarios is more extensive than experimentally tested to-date. Figure 1.1f provides examples of potential IoT applications of the PEC in: (i) vehicle sensing (thermal charging with vehicle start-up) [3]; (ii) flight monitoring (thermal charging with altitude) [27]; and (iii) agricultural sensing (thermal charging with diurnal temperature fluctuations)[34]. Each scenario presents different values of  $dT/dt$  ( $\approx 5$  s-12 h) and  $\Delta T$  (few°C to several 10’s of°C) affecting PEC energy harvesting and storage. Before embarking on the fabrication of PECs for these applications, it is worthwhile to probe the design space through simulation to identify preferred approaches for coupling cell design parameters and application. Lumped parameter models provide a means of rapidly exploring PEC designs to increase thermal-to-electrochemical energy conversion in different thermal charging scenarios.

The remainder of this thesis is structured as follows. Chapter 2 introduces the developed equivalent circuit model. Chapter 3 outlines the experimental methods used for parameter extraction. Chapter 4 presents validation results comparing the circuit model to experimental OCP data. Chapter 5 conducts an exploration of performance based on the developed model. Finally, Chapter 6 summarizes key insights and proposes directions for future research.

## CHAPTER 2

### MODEL

The equivalent circuit model developed in this thesis builds upon established supercapacitor models to represent both energy storage and ion transport processes in the PEC [13, 16, 25, 26, 31].

#### 2.1 The Equivalent Circuit

Figure 2.1a and b illustrate the equivalent circuit model used to represent the PEC. The model consists of a modified Randle's circuit representing the EDLC and a current source,  $I_p$ , representing the pyroelectric separator. The modified Randle's circuit consists of a series resistance ( $R_s$ ) and two parallel RC branches representing high-frequency ( $R_1$ ,  $CPE_1$ ) and low-frequency ( $R_2$ ,  $CPE_2$ ) behavior. Capacitive elements are represented as constant phase elements (CPEs), with impedance governed by associated values of  $Q$  and  $\alpha$ . High-frequency behavior is governed by charge transfer resistance and double layer capacitance of large pores. Low-frequency behavior is governed by complex factors which may include diffusion, charge redistribution, leakage, and double layer capacitance in small pores [13, 16, 18, 19, 23, 25, 26, 31, 33].

The direction of the current source  $I_p$  can be varied to simulate different orientations of pyroelectric separator polarization with respect to the supercapacitor anode and cathode. When  $I_p$  is directed to increase cell voltage upon heating, the circuit model represents the pyroelectric separator in "cathode-facing" ("aiding") orientation [21]. When  $I_p$  is directed to decrease cell voltage upon heating, the circuit model represents the pyroelectric separator in "anode-facing" ("hindering") orientation. The equivalent circuit model reduces to a simple EDLC simulation when  $I_p = 0$ . In this case, the circuit model simulates the "thermal" response of the cell, with changes in cell voltage arising from temperature-dependent values of circuit elements without pyroelectric contributions. This is equivalent to heating and/or cooling an EDLC with a non-pyroactive separator, or conducting electrochemistry

measurements with a pyroactive separator at constant temperature.

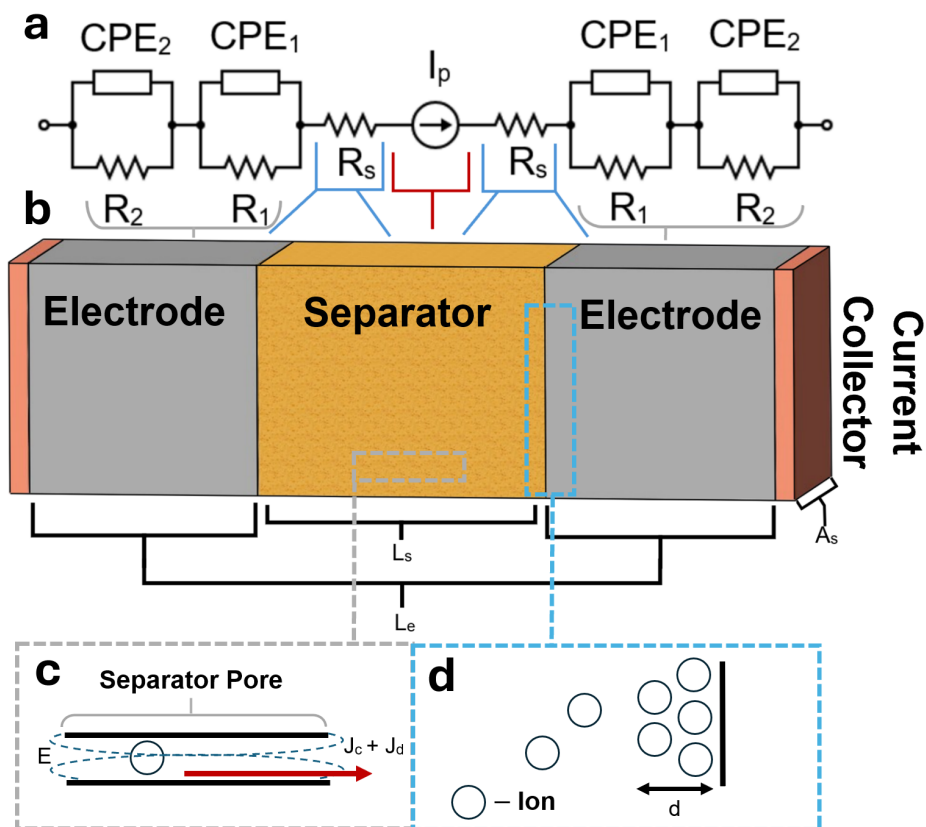


**Figure 2.1.** a) Equivalent circuit model of the PEC based on a modified Randle's circuit ( $R_s$ ,  $R_1$ ,  $R_2$ ,  $CPE_1$ , and  $CPE_2$ ) and a pyroelectric current source ( $I_p$ ). b) Physical representation of how the circuit fits into the cell as well as the cell's geometric configuration ( $L_s$ ,  $L_e$ , and  $A_s$ ). c) The conduction ( $J_c$ ) and displacement ( $J_d$ ) current densities caused by the pyroelectric electric field ( $E$ ) moves ions through pores in the separator. d) The ions are stored in the double layer at the electrode-electrolyte interfaces with a Debye screening length of  $d$ .

Together, these circuit elements provide a detailed representation of the PEC's dynamic behavior, capturing both fast and slow processes essential for energy storage.

A critical distinction in our PEC model compared to classical supercapacitors is the inclusion of a pyroelectric current source ( $I_p$ ) at the center of the circuit. Unlike conventional pyroelectric models, in the PEC, the pyroelectric separator's electric field directly drives ionic transport through its porous structure and toward the electrodes (Figure 2.1c). This mechanism enables the direct conversion of thermal energy into stored electrochemical energy as ions move to the electrode-electrolyte double layer interfaces (Figure 2.1d). This

operational principle arises due to the separator's immersion in electrolyte, maintaining an open circuit condition rather than the traditional short-circuit condition used in standard pyroelectric setups [7, 11]. Incorporating this current source accurately captures the unique functionality of the PEC, where thermal energy conversion directly facilitates ion movement and enhances electrochemical energy storage.

## 2.2 Theory

Each element in the equivalent circuit model (Figure 2.1a) corresponds to a specific physical or behavioral characteristic of the PEC (Figure 2.1b). Many of these elements have established theoretical equations derived from mathematical models or experimental observations that allow for the calculation of their expected values based on existing research.

### 2.2.1 Resistances

There are three primary resistances that need to be calculated (see Fig 2.1): the series resistance, the high-frequency charge transfer resistance, and the low-frequency diffusion/leakage resistance. The series resistance ( $R_s$ ) is primarily influenced by the electrolyte as it permeates through the porous separator and electrode. To facilitate independent optimization of the separator and electrode parameters, the total series resistance is modeled as the sum of two distinct resistive components, representing the physical separation of these regions within the cell:

$$R_s = \frac{L_e}{\sigma A_e} + \frac{L_s}{\sigma A_s}, \quad (2.1)$$

where  $L_e$  represents the thickness of the electrodes encompassing the electrolyte, excluding the separator and current collectors, and  $L_s$  accounts for the separator thickness. The term  $\sigma$  denotes the ionic conductivity of the electrolyte, while  $A_e$  and  $A_s$  correspond to the cross-sectional surface area of the porous electrodes and separator. In our experimental case, the PEC was a porous PVDF-BT separator with  $0.5MNa_2SO_4$  electrolyte.

The high-frequency charge transfer resistance ( $R_1$ ) represents the fast acting resistance at the electrode-electrolyte interface, and while it can be calculated by an equation, some variables require observation to characterize it fully. Known constants such as the univer-

sal gas constant ( $R_g$ ), absolute temperature ( $T$ ), and Faraday's constant ( $F$ ) exist within the charge transfer resistance equation. Certain experimental values - such as the exchange current ( $i_0$ ), determined from fitting the PEC's cyclic voltammetry (CV) data, and the expected number of electrons transferred ( $n$ ), estimated based on the electrode reactions - are also needed to solve the equation directly:

$$R_1 = \frac{R_g T}{n F i_0}. \quad (2.2)$$

Calculating low-frequency diffusion/leakage resistance ( $R_2$ ) is inherently complex due to various non-idealities in the system, such as manufacturing defects, power management inefficiencies, and electrolyte properties [13, 16, 18, 23, 25, 26, 31, 33]. At least one study ran by Kang et al. requires the knowledge of activation energies within the cell at various temperatures to understand how this resistance changes with temperature [19]. Rather than being derived from a single variable, this low-frequency resistance is typically observed as the result of a combination of these factors, and can significantly impact the performance of supercapacitors. Although it is non-trivial to calculate  $R_2$  directly, its effects on performance can be quantified through experimental observations.

### 2.2.2 Capacitances

The circuit uses  $Q$  to represent the capacitive effect of constant phase elements (CPEs) rather than  $C$  for capacitance because the PEC exhibits an inherent non-ideal behavior. While  $C$  is traditionally used for ideal capacitors that follow simple relationships between charge and voltage, real-world supercapacitors, such as the PEC, exhibit deviations from this ideal behavior and require the use of a more nuanced solution in estimating capacitances, especially around the double layer [14, 37], in order to observe proper fitting between model and experimental data. The use of constant phase elements accounts for these non-idealities within the element's impedance. The impedance of a CPE is  $Z_Q = \frac{1}{Q(j\omega)^\alpha}$ , where  $Q$  is the capacitance given by Equation 2.3 or Equation 2.6. Here,  $\alpha$  ranges from 0 to 1, with 0 representing the impedance of a perfect resistor and 1 representing a perfect capacitive impedance [8]. As such, all non-ideal capacitances in this thesis are denoted by  $Q$  to reflect the non-ideal characteristics of the device, while  $C$  will be used when assuming ideal capacitive conditions.

Within our circuit, there are two capacitances that make up the total capacitance of the PEC: high-frequency and low-frequency double layer capacitance. The high-frequency double layer capacitance ( $Q_1$ ) reflects the capacity to store charge in the electric double layer at the interface of the electrolyte and the active electrode layer for quick time periods. This high-frequency capacitance is calculated similarly to static plate capacitances using the material properties of the electrolyte and thickness of the double layer. We use the dielectric permittivity of the electrolyte ( $\epsilon_e$ ), the active surface area of the electrode ( $A_{e,act}$ ), and Debye screening length for the double layer thickness ( $d$ ) in our equations,

$$Q_1 = \frac{\epsilon_e A_{e,act}}{d} \quad (2.3)$$

$$d = \sqrt{\frac{\epsilon_e k_b T}{2e^2 N_A I'}} \quad (2.4)$$

where  $k_b$  is the Boltzmann constant,  $T$  is absolute temperature,  $e$  is the elementary charge,  $N_A$  is Avogadro's number, and  $I$  is the ionic strength of the electrolyte.

The low-frequency double layer capacitance ( $Q_2$ ), also referred to as distributed double layer capacitance or pseudocapacitance, represents the charge storage capability of the electrode material itself and is associated with diffusion control of the ions through micropores in the electrode [35, 42]. As noted by Guo et al. [15], this low-frequency capacitance serves as a metric for evaluating the charge storage capability of electrode materials, particularly in the context of optimizing supercapacitor performance. In this analysis, the low-frequency capacitance is estimated using gathered data from cyclic voltammetry (CV). The expected value of low-frequency capacitance is derived by subtracting the calculated high-frequency capacitance from the experimentally measured total capacitance of the supercapacitor,

$$Q_2 = Q_{total} - Q_1. \quad (2.5)$$

The total capacitance can be calculated from the CV plot where the sum of the charge and discharge areas ( $A_c, A_d$ ) is divided by the scan rate ( $\nu$ ) and the voltage window ( $\Delta V$ ) [25],

$$Q_{total} = \frac{A_c + A_d}{v\Delta V}. \quad (2.6)$$

### 2.2.3 Pyroelectric Current Source

The total pyroelectric current ( $I_p$ ) generated by the separator upon experiencing a temperature change is the sum of the conduction current density ( $J_c$ ) and the displacement current density ( $J_d$ ), multiplied by the separator surface area,  $A_s$  (Equation 2.7):

$$I_p = (J_c + J_d)A_s \quad (2.7)$$

$A_s$  is a function of the surface area of the cell,  $A$ , and  $\gamma_s$  (Equation 2.8):

$$A_s = A(1 - \gamma_s) \quad (2.8)$$

$J_c$  (Equation 2.9) is governed by the electric field,  $E$ , that arises when the pyroelectric separator dipoles shift their alignment due to a temperature change,  $dT$  (Equation 2.10):

$$J_c = Ek\sigma \quad (2.9)$$

$$E = \frac{pdT}{\epsilon_s} \quad (2.10)$$

The parameter  $k$  in Equation 2.9 is a fitting factor that accounts for the screening effect of ions within the pores of the pyroelectric separator. During heating and cooling, mobile ions migrate and accumulate at the interfaces around and within the porous separator, particularly along pore walls and outer edges. This accumulation creates a localized charge distribution that counteracts the pyroelectric field, reducing the net driving force for ion migration as illustrated in Figure 2.2[2, 20].

While theoretical models of pyroelectric fields in solid-state materials assume an un-screened response, the presence of an electrolyte introduces additional complexities due to electrostatic interactions, charge redistribution, and pore geometry effects. A  $k$  value of  $2.4 \times 10^{-8}$  was determined through fitting the equivalent circuit model to experimental data, providing the best agreement across electrochemical techniques. However,  $k$  is not derived from first principles. Further investigation is needed to characterize the effects of

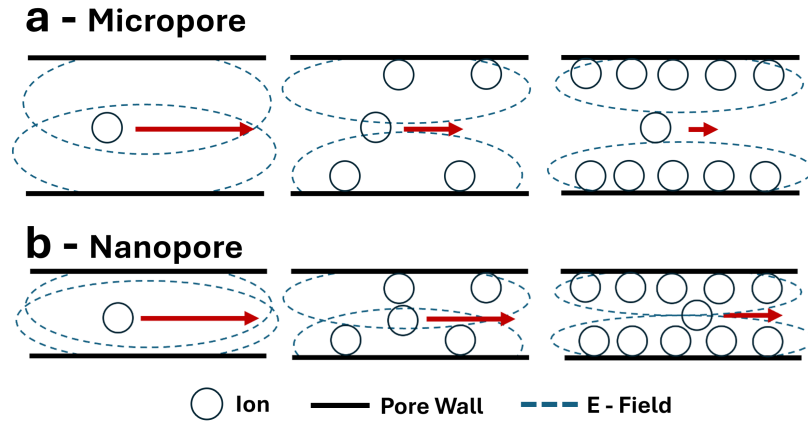


**Figure 2.2.** A simplified illustration of ions passing through a a) micropore versus a b) nanopore and how the screening affects ion movement through the pore. The farther from the pore wall, the lower the electric field becomes and the less influence it has on ion movement.

temperature, electrolyte conductivity, and separator geometry on  $k$ . Future work should aim to characterize the dependence of  $k$  on these parameters and develop a more direct method for calculating it from material properties rather than relying solely on empirical fitting.

Equation 2.10 assumes that the temperature is spatially uniform throughout the pyroelectric material and that the material is in open circuit condition [38].

$J_d$  in Equation 2.11 arises from the electrical displacement ( $dD$ ) (Equation 2.12) within the pyroelectric separator and is a function of the rate of change of temperature:

$$J_d = \frac{dD}{dt} \quad (2.11)$$

$$dD = \epsilon_s dE + pdT \quad (2.12)$$

For small values of  $dT/dt$  (*i.e.* less than  $10^\circ\text{C/s}$ ),  $J_d$  becomes negligible and the pyroelectric current is dominated by the conduction current,  $J_c$ .

## CHAPTER 3

### PARAMETER EXTRACTION

Initial parameters for the equivalent circuit model were extracted from EIS, CV, and amperometry measurements. Details of these experimental measurements are described in [21]. The experimental PEC consisted of commercially-available activated carbon electrodes (90  $\mu\text{m}$  thickness) and copper current collectors. The separator was porous PVDF-BT (60  $\mu\text{m}$  thickness, 65% porosity). Electrodes and separator were saturated with 0.5M  $\text{Na}_2\text{SO}_4$  electrolyte. EIS (0.1 Hz-100 kHz) and CV measurements (100 mV/s, 0-250 mV) were conducted at 20°C and 50°C static temperatures. Amperometry experiments were conducted by heating the cell between 20°C and 50°C while maintaining a constant cell voltage of 120 mV. Amperometry experiments were conducted with the pyroelectric separator in “cathode-facing” (“aiding”) orientation and “anode-facing” (“hindering”) orientations. Amperometry experiments were also conducted with a non-pyroelectric (Celgard) separator to measure “thermal” (non-pyroelectric) effects.

Equivalent circuit model simulations were implemented in MATLAB. Least squares fitting was used to obtain the best agreement between simulation and experimental data across EIS, CV, and amperometry measurements. Table 3.1 provides equivalent circuit model parameters that achieve a best fit with the experimental PEC across all measurements and temperatures while Table 3.2 provides a summary of the geometric, material, and electrical properties extracted for each element. Parameters were either directly measured or derived based on experimental data and known material properties of the PEC. Figure 3.1 provides the corresponding best fit curves for EIS (Figures 3.1a, b), CV (Figure 3.1c), and amperometry (Figure 3.1d) measurements. Capacitive and resistive circuit values in Table 3.1 are specified at 20°C and 50°C. These values produce EIS and CV curves at their respective temperatures. Pyroelectric current is absent in EIS and CV simulations (*i.e.*  $I_p = 0$  in Figure 3.1a-c). Euclidean distance error calculations for EIS and

CV fits confirm that the equivalent circuit model simulations closely match experimental data, with deviations remaining within 2% at both high and low temperatures. Amperometry simulations were used to extract  $I_p$ . Linear interpolation was used to account for changing values of  $R_s$ ,  $R_1$ ,  $R_2$ ,  $CPE_1$ , and  $CPE_2$  as the cell temperature was varied from 20-50-20°C. Euclidean distance error calculations for amperometry indicate 4.60% error for the “thermal” fit, 3.86% error for the “hinder” fit, and 11.45% error for the “aid” fit. The relatively large error for the “aid” fit is attributed to experimental artifacts producing an unexplained drop in  $\Delta i$  around the maximum cell temperature (Figure 3.1d).

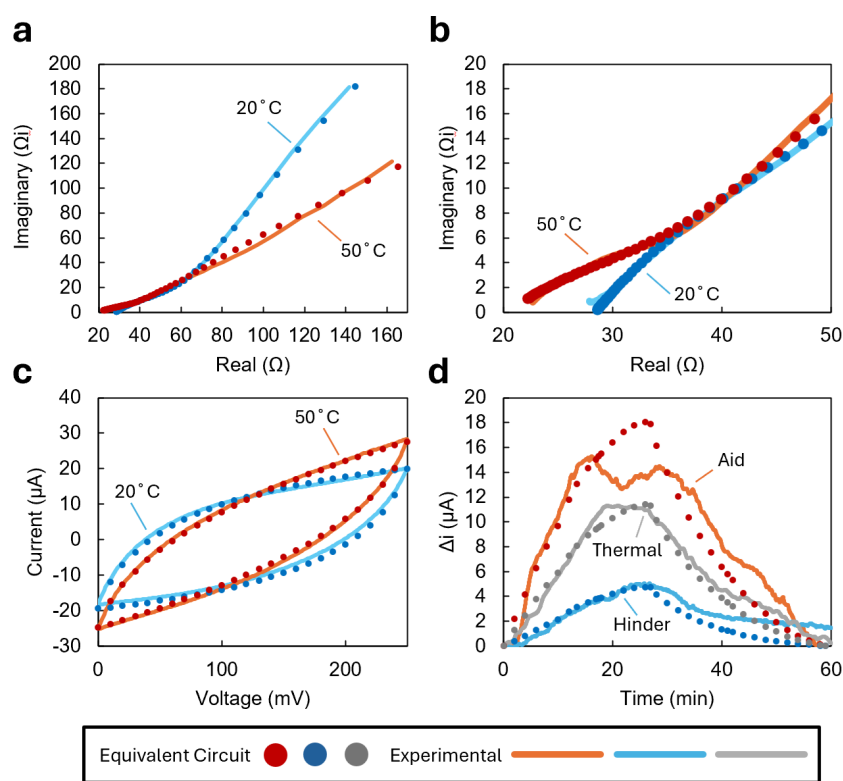


**Figure 3.1.** Equivalent circuit model best fit with experimental PEC. a) EIS fit at 20°C and 50°C. b) CV fit at 20°C and 50°C. c) Amperometry fit for a 20-50-20°C temperature cycle. Experimental results adapted from [21].

The inclusion of the pyroelectric current ( $I_p$ ) in the table highlights its behavior during the thermal cycling process. The value of  $6.53 \mu A$  represents the reversible nature of the current, where an increase in temperature from 20°C to 50°C results in a positive response, and a return to 20°C yields a symmetrical negative effect.

**Table 3.1.** List of circuit elements and their values at 20°C and 50°C.

<b>Circuit element</b>	<b>20</b>	<b>50</b>
$R_s$ ( $\Omega$ )	14.23	10.25
$R_1$ ( $\Omega$ )	20.00	9.37
$Q_1$ ( $S/s^n$ )	0.0073	0.0070
$\alpha_{dl}$	0.520	0.368
$R_2$ ( $\Omega$ )	1000	845
$Q_2$ ( $S/s^n$ )	0.0143	0.0137
$\alpha_m$	0.793	0.522
$I_p$ ( $\mu A$ )	6.53	

**Table 3.2.** List of parameters, extracted values, and affected equivalent circuit elements.

<b>Parameter</b>	<b>Value(s) (20°C/50°C)</b>	<b>Element Affected</b>
$L_e$	90 $\mu m$	$R_s$
$L_s$	60 $\mu m$	$R_s$
$A$	36 $cm^2$	$R_s, I_p$
$I$	1.5 $mol/L$	$R_1$
$\sigma$	0.0133/0.012 $S/m$	$R_s, I_p$
$i_0$	0.00126/0.00297 $A$	$R_1$
$p$	59 $\mu C/m^2K$	$I_p$
$\gamma_s$	65%	$I_p, R_s$
$\epsilon_e$	70/60.24	$Q_1$
$\epsilon_s$	11	$I_p$

## CHAPTER 4

### MODEL VALIDATION

The equivalent circuit model's ability to represent PEC behavior was validated by comparing circuit model OCP simulations *vs.* experimental measurements and an existing COMSOL model [21]. Unlike EIS, CV, and amperometry measurements, OCP experimental data was not used for equivalent circuit model parameter extraction. OCP measurements thus provide an independent assessment of the equivalent circuit model's ability to represent PEC device physics under thermal cycling conditions. OCP simulations using the equivalent circuit model were conducted using ideal capacitors in place of CPEs, allowing us to solve standard RC circuit differential equations in the time domain. To the best of our knowledge, OCP simulations of supercapacitors incorporating CPE-based equivalent circuit models have not been reported. While various methods exist for determining effective capacitances from CPEs [10,17], these approaches typically rely on frequency-domain data and are tailored to specific circuit configurations that differ from our own. As a result, directly incorporating CPEs into time-domain OCP simulations remains incompatible within our current modeling framework. Therefore, from this point on, we will refer to the high- and low-frequency capacitances as ideal capacitances  $C_1$  and  $C_2$ , respectively. Electrolyte conductivity,  $\sigma$ , affecting  $I_p$  and  $R_s$  (see Equations 2.1 and 2.7-2.10), was treated as temperature-dependent using the general equation of ionic conductivity and temperature-dependent diffusivities of  $\text{Na}^+$  and  $\text{SO}_4^{2-}$  ions [9,36].

Figure 4.1a compares OCP simulations using the equivalent circuit model and COMSOL Multiphysics *vs.* experimental measurements for a 20-30-20°C thermal cycle. The nominal time for one thermal cycle was 40 min [21]. Due to slight differences in the thermal cycle time between equivalent circuit model, COMSOL simulation, and experiment, OCP results in Figure 4.1a are normalized by number of cycles. OCP is plotted as " $\Delta\text{OCP}$  (mV)" to account for the small, non-zero starting OCP for the experimental cell [21]. The effect of

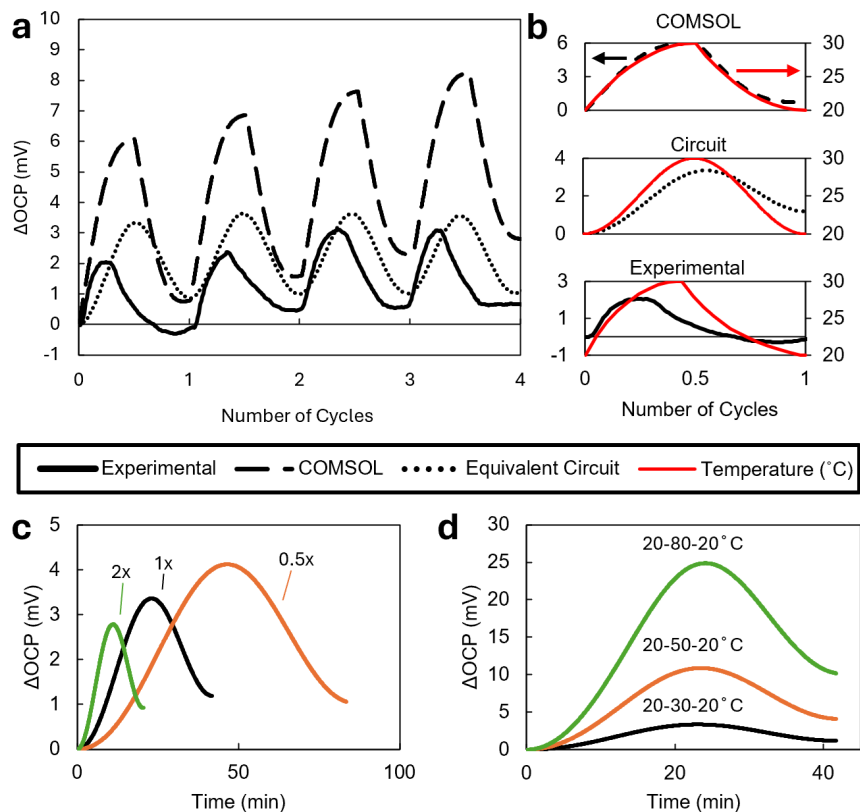
starting OCP on equivalent circuit model predictions of  $\Delta\text{OCP}$  is explored in-depth in the Supporting Information within Appendix A (Figure S1, S2).

Figure 4.1a shows that the equivalent circuit model produces the expected rise and fall in OCP in response to a thermal input. The equivalent circuit model provides better agreement with experimental results *vs.* the COMSOL simulation when considering the magnitude of  $\Delta\text{OCP}$ . This is likely due to the COMSOL simulation neglecting diffusion resistance and leakage current, both of which are accounted for in the equivalent circuit model. All three curves in Figure 4.1a show a net increase in  $\Delta\text{OCP}$  after four cycles, with the equivalent circuit model again displaying better agreement with experimental results *vs.* the COMSOL simulation.

Differences in the shapes of OCP profiles in Figure 4.1a can be explained by comparing COMSOL, equivalent circuit model, and experimental  $\Delta\text{OCP}$  results *vs.* their thermal inputs for a single cycle (Figure 4.1b). COMSOL  $\Delta\text{OCP}$  values track the simulated temperature profile exactly, as expected for a flat plate model. The equivalent circuit model thermal input was approximated as a sinusoidal temperature change. This difference in thermal input explains some of the differences in  $\Delta\text{OCP}$  curve shapes observed in Figure 4.1a. The equivalent circuit model follows its temperature profile with a small degree of lag which we attribute to the RC time constant of the model. Differences in temperature profile *vs.*  $\Delta\text{OCP}$  for the experimental cell may be due to a number of factors, including location of temperature measurement (*i.e.* water bath *vs.* the pyroelectric separator itself) and/or leakage and diffusion effects.

The equivalent circuit model's ability to predict changes in OCP for varying  $dT/dt$  inputs is plotted in Figure 4.1c, where "1x" refers to the  $dT/dt$  rate associated Figure 4.1a, and "2x" and "0.5x" are twice and half this rate, respectively. The equivalent circuit model predicts that a 1x rate cycle repeated two times, or a 2x rate cycle repeated four times, would produce the same  $\Delta\text{OCP}$  as a one cycle at 0.5x rate. This is consistent with the constitutive equations of pyroelectrics, which predict net energy harvested dependent on  $\Delta T$  rather than  $dT/dt$ . Figure 4.1d plots equivalent circuit model predictions of  $\Delta\text{OCP}$  for three different temperature changes: 20-30-20° C, 20-50-20°, and 20-80-20° C (1x rate). The results are consistent with increasing  $\Delta T$  producing greater PEC energy harvesting and storage. We note that the rate predictions of the equivalent circuit model (Figure 4.1c)

differ somewhat from those of the COMSOL simulation (for details see [21]). We attribute these differences to the equivalent circuit model more accurately representing real-world RC time constants of a porous electrode *vs.* the flat plate approximation of the COMSOL simulation.



**Figure 4.1.** Model validation: a) A comparison of experimental, COMSOL Multiphysics simulation, and equivalent circuit model  $\Delta OCP$  for a 20-30-20  $^{\circ}C$  thermal cycle repeated four times. b) Single-cycle comparison of part (a) results with associated temperature profiles. c) Equivalent circuit model  $\Delta OCP$  predictions for the same  $\Delta T$  (20-30-20  $^{\circ}C$ ) but different  $dT/dt$  rates. The “1x” rate corresponds to the results shown in (a) and (b). d) Equivalent circuit model  $\Delta OCP$  predictions for the same  $dT/dt$  rate but different  $\Delta T$  values.

## CHAPTER 5

### MODEL-BASED PERFORMANCE EXPLORATION

The exploration of the PEC focuses on its energy density by analyzing the noted vital design parameters and material properties. Using the equivalent circuit model and experimental data, we assess how variations in parameters (noted in Table 5.1) affect the PEC's energy density.

Table 5.1 lists the cell design parameters explored, which include: separator thickness  $L_s$ , separator porosity  $\gamma_s$ , electrolyte conductivity  $\sigma$ , separator pyroelectric coefficient  $p$ , and separator relative permittivity  $\epsilon_s$ . Design parameters were changed one at time, with all other parameters held constant at the "experimental cell" values specified in Table 5.1. Experimental cell values of  $L_s$ ,  $\gamma_s$ ,  $p$ , and  $\epsilon_s$  are as reported in [21]. The experimental cell value of  $\sigma$  was derived from EIS measurements of  $R_s$ , and found to agree well with literature 0.5 M Na<sub>2</sub>SO<sub>4</sub> [39].

**Table 5.1.** Parameter exploration

Parameter	Experimental Cell	Circuit Model Range	Circuit Element Affected
$L_s$	60 $\mu m$	1-500 $\mu m$	$R_s$
$\gamma_s$	65%	20-80%	$R_s, I_p$
$\sigma$	0.0133 S/m	0.0001-0.1 S/m	$R_s, I_p$
$p$	59 $\mu C/m^2K$	1-1000 $\mu C/m^2K$	$I_p$
$\epsilon_s$	11	1-1000	$I_p$

The "circuit model range" column of Table 5.1 lists the range over which cell design parameters were varied in the equivalent circuit model. Separator design parameters ( $L_s$ ,  $\gamma_s$ ) were varied over a larger range than commonly used in commercial electrochemical cells to account for the dual functionality of the separator as ion conductor and pyroelectric energy harvester. Data from previous studies indicates that supercapacitor separators have been

fabricated with  $\gamma_s$  ranging from 10% to 90% [1]. The range of  $\sigma$  values is typical of aqueous and organic electrolytes reported in literature [22]. Separator pyroelectric coefficient and permittivity were varied over ranges typically reported for pyroelectric materials [5,7]. Equivalent circuit model elements affected by the design parameters in Table 5.1 include  $I_p$  and  $R_s$ .

Circuit element values not affected by the design parameters listed in Table 5.1 ( $R_1$ ,  $R_2$ ,  $C_1$ ,  $C_2$ ) were kept constant at the values listed in Table 3.1. All capacitors were treated as ideal ( $\alpha_1$ ,  $\alpha_2 = 1$ ).

For each value of a cell design parameter in Table 5.1, the associated values of equivalent circuit model elements  $I_p$  and  $R_s$  were calculated.  $\Delta OCP$  was simulated based on a 20-30-20 °C temperature change (40 min thermal cycle). Energy density for one thermal cycle normalized by area,  $U_A$  was then calculated based on the cycle time,  $t$ , and the total cell impedance,  $Z$  (Equation 5.1):

$$U_A = \frac{1}{A} \int_0^t \frac{\Delta OCP^2}{Z} dt \quad (5.1)$$

## 5.1 Cell Design Parameters

Figure 5.1a examines the influence of separator thickness ( $L_s$ ) and electrolyte conductivity ( $\sigma$ ) on PEC energy density. Both parameters contribute to the series resistance,  $R_s$  (Equation 2.1). With a separator porosity of 65% (Table 5.1, “experimental cell” value), PEC energy density exhibits greater sensitivity to  $\sigma$  than to  $L_s$ . This is likely due to the dual effect of  $\sigma$  on enhancing both the conduction current density,  $J_c$  (Equation 2.9), and reducing  $R_s$  (Equation 2.1), thereby improving ion transport efficiency throughout the separator and the entire cell. The design implications of Figure 5.1a are twofold: (1) high-conductivity aqueous electrolytes are preferred for optimal PEC performance, and (2) area-based energy density remains largely unaffected by variations in  $L_s$ , meaning higher  $L_s$  values can be accommodated without significant energy loss.

For the experimental PEC, the estimated electrolyte conductivity ranged from 1.14 to 2.81 mS/m, with a MacMullin number between 5 and 12. These values, calculated using methods outlined by Landesfeind et al., are comparable to those found in many existing supercapacitors [22, 24]. However, further improvements could be achieved through elec-

trolyte selection or separator engineering strategies that enhance  $\sigma$  without compromising mechanical stability or increasing leakage.

Figure 5.1b illustrates the effects of  $\epsilon_s$  and  $p$  on PEC energy density. Data points corresponding to specific pyroelectric materials (ZnO, PVDF, NaNO<sub>2</sub>, PVDF-BT, LiTaO<sub>3</sub>, PZT) are indicated on the 2D surface plot and are further set out in Table 5.2. Separator materials with high  $p$  and low  $\epsilon_s$  provide the highest values of energy density. This is due to the PEC utilizing the generated electric field,  $E$ , rather than the displacement field of the pyroelectric while in open circuit condition. The pyroelectric coefficient ( $p$ ) plays a central role in determining the strength of the electric field generated within the separator in response to temperature changes. The coefficient,  $p$ , directly influences the amount of current in the circuit as seen in Equations 2.7-2.10.

The separator's relative permittivity ( $\epsilon_s$ ) influences the electric field distribution and, consequently, the generated current. For slow cycle times, where electrical displacement is negligible, the primary factor is the electric field ( $E$ ), which is inversely proportional to  $\epsilon_s$ . Higher  $\epsilon_s$  values reduce  $E$  by more effectively screening the polarization effects that drive charge separation, leading to less efficient ion transport. As a result, materials with high permittivity require greater pyroelectric coefficients to compensate for this screening effect. This limitation is particularly evident in PZT, a strong pyroelectric material whose high permittivity diminishes its effective field within the PEC, despite its favorable pyroelectric coefficient.

Separator porosity ( $\gamma_s$ ) governs  $R_s$  (Equation 2.1) and  $I_p$  (Equations 2.7 and 2.8). Figure 5.1c indicates that PEC energy density is improved when the areal fraction of separator active material is increased (*i.e.* smaller  $\gamma_s$ ), despite the corresponding increase in  $R_s$ . Manufacturing considerations are also important when designing a pyroelectric separator for the PEC. Many high-performing pyroelectric materials are rigid and brittle, requiring extra engineering to form them into suitable (*i.e.* flexible and porous) separators for the PEC. The improvement in PEC energy density with lower separator porosity is likely a benefit for separator manufacturing for many pyroelectric materials.

Figure 5.1d compares the magnitude of each design variable's effect size on PEC energy density. Data points correspond to the average value of each variable range in Table 5.1; bar lengths correspond to the full "circuit model range".  $L_s$  is not included due to its

negligible effects as illustrated in Figure 5.1a. It is seen that  $\gamma_s$  has the least effect on PEC energy density, with separator material properties, most notably  $p$ , having a much more significant impact on cell energy density.

The red dashed line in Figure 5.1d corresponds to the low-power IoT application energy density benchmark of  $100 \mu\text{J}/\text{cm}^2$ . Overall energy density values in Figure 5.1d are low compared to the target as they are based on the experimental cell of Kowalchik *et al.* [21], with one variable at a time design adjustments. Circuit model design parameter exploration that supports multi-variable optimization is expected to greatly improve the energy density values of Figure 5.1d, and is the subject of future work. At this early stage of circuit model-based parameter exploration, it is encouraging to see that PEC energy densities well exceeding the IoT benchmark can be achieved with the current experimental cell if higher  $p$  separator materials are implemented.

As shown in Figure 5.1d, by finding a material with higher  $p$  (around and above  $500 \mu\text{C}/\text{m}^2\text{-K}$ , on the higher end of the explored range in Table 5.1), the model predicts energy densities well above the  $100 \mu\text{J}/\text{cm}^2$  benchmark while utilizing a  $\Delta T$  of  $10^\circ\text{C}$ . Such materials exist including PZN-PT and PMN-PT single crystals and a few bulk ceramics, while many thin films and polymers composites come close to this threshold [32]. The pyroelectric coefficient requirement can be lower for larger  $\Delta T$  ranges. These results bring the PEC much closer to the  $100 \mu\text{J}/\text{cm}^2$  benchmark and the generally accepted range of 50 to  $500 \mu\text{J}$  per thermal cycle for a given IoT data logging and transmission event, showing that the optimization strategy has the opportunity to enhance energy harvesting capabilities.

**Table 5.2.** A comparison of known pyroelectric materials and their calculated energy densities within the equivalent circuit model. Pyroelectric coefficients and permittivities were supplied by [7, 21].

<b>Material</b>	$p(\mu\text{C}/(\text{m}^2\text{K}))$	$\epsilon_s$	$U_A(\mu\text{J}/\text{cm}^2)$
<i>PVDF – BT</i>	59	11	3.52
<i>PVDF</i>	27	9	1.91
<i>PZT</i>	380	290	6.35
<i>LiTaO<sub>3</sub></i>	176	47	4.35
<i>ZnO</i>	9.4	11	0.99
<i>NaN<sub>2</sub>O</i>	40	4	6.41

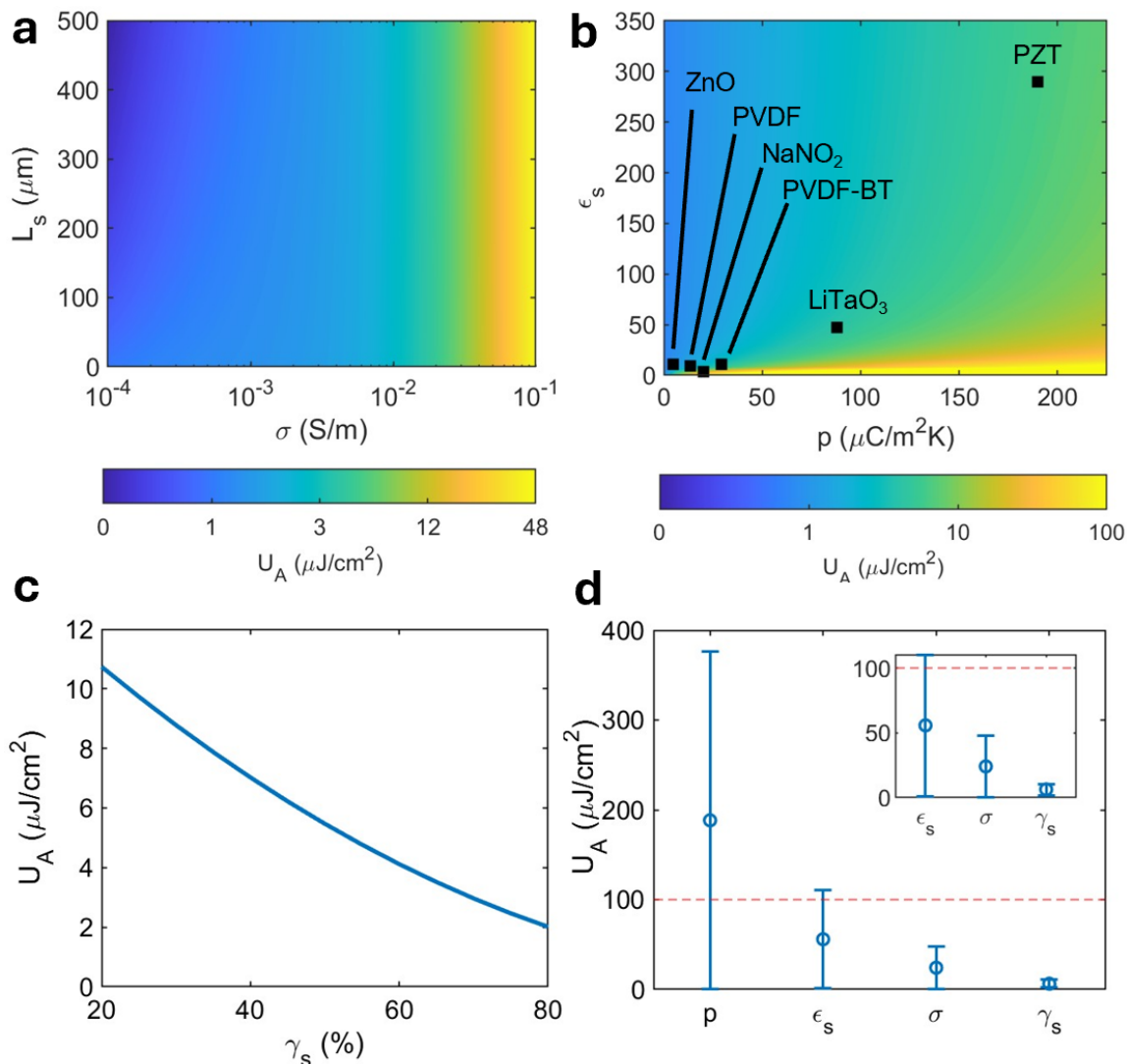


**Figure 5.1.** Parameter exploration. a) 2D surface plot illustrating the effects of  $L_s$  and  $\sigma$  on PEC energy density. b) 2D surface plot of  $p$  vs.  $\epsilon_s$  effects on PEC energy density. c) Increase in PEC energy density with decreasing  $\gamma_s$ . d) Effect sizes of the design variables explored in Table 2. Dashed line: low-power IoT application benchmark.

By comparing all these parameters and assessing their relative impacts on the energy density, we can prioritize the design changes that will most significantly enhance PEC performance. First, priority should be given to selecting a separator with an increased pyroelectric coefficient and a decreased relative permittivity, with the pyroelectric coefficient acting as the more influential factor. Next, optimizing the conductivity of the electrolyte is crucial, while carefully considering the cell geometry (such as porosity and cross-sectional

area), as this is hypothesized to affect the fitting factor used by the model. Finally, adjustments to the overall length and thickness of the cell, though less impactful, should still be evaluated and minimized where necessary to further improve performance.

## 5.2 Thermal charging rate

Circuit elements  $C_1$  and  $R_1$  govern the high-frequency behavior of the PEC with an RC time constant  $\tau_1 < 0.15$  s. Circuit elements  $C_2$  and  $R_2$  govern the low-frequency behavior of the PEC. Their associated time constant  $\tau_2$  is the primary factor determining the overall time constant of the cell.

Table 5.3 and Figure 5.2 explore the effects of  $C_2$ ,  $R_2$ , and  $\tau_2$  on PEC energy density for thermal cycles of 30 s to 24 h. For any given thermal cycle length, there is an optimum value of  $\tau_2$  that maximizes energy density. This is shown in Figure 5.2a for the case of a 40 min thermal cycle, which reaches a maximum energy density at  $\tau_2 \approx 205$  min. For all thermal cycle lengths listed in Table 5.3, a  $\tau_2$  value  $\approx 3$ -5x the thermal cycle length maximizes energy density within the circuit. At this value, leakage effects are reduced while limiting overall cell impedance,  $Z$  (Equation 5.1). In low-power applications, an extended time constant allows the EDLC to gradually accumulate and maintain energy harvested through temperature changes.

Low-frequency branch simulations further indicate that optimum values of  $\tau_2$  are best achieved with small values of  $C_2$  and large values of  $R_2$  (Figure 5.2b). In EDLC equivalent circuit models,  $C_2$  represents capacitive charge storage predominantly within micropores. At a first approximation, PEC electrodes with smaller quantities of micropores and higher leakage resistance are suggested for maximizing energy density. Optimum values of  $C_2$  are still larger than  $C_1$  for all simulations. The small value of  $C_1$  vs.  $C_2$  in Table 3.1 indicates that overall PEC capacitance is dominated by high-frequency, fast-charging surfaces represented by  $C_1$ . The larger capacitance  $C_2$  may not be fully utilized due to the slow charging behavior of the low-frequency branch.

## 5.3 A Note on Temperature Difference

The temperature dependence of different elements should be noted for the importance of this optimization process. Large-temperature windows are typically desired for the ba-

**Table 5.3.** Optimum values of  $\tau_2$  and  $R_2$  (with corresponding  $U_A$ ) for varying thermal cycle lengths.

Thermal Cycle	$\tau_2$	$R_2$ (k $\Omega$ )	$U_A$ ( $\mu\text{J}/\text{cm}^2$ )
30 s	2.0 min	8.7	315.18
1 min	2.7 min	11.5	305.27
15 min	57.8 min	247	313.45
40 min	204.9 min	880	302.48
3 h	9.0 h	2310	309.55
12 h	36.3 h	9326	309.93
24 h	83.8 h	21544	313.38

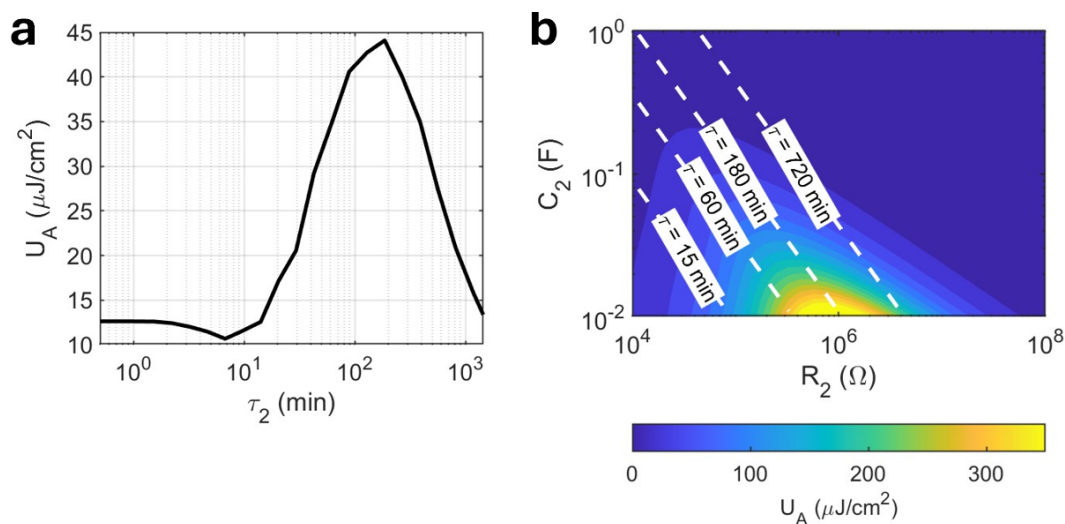


**Figure 5.2.** Low-frequency RC simulations for a 40 min thermal cycle length. a) Effect of  $\tau_2$  on cell energy density. A maximum value of  $U_A$  is reached at a  $\tau_2$  of 205 min. b) Low-frequency RC branch parameters and their effect on  $U_A$  for a 40 min thermal cycle.

sics of pyroelectric technology to work. However, one must also take into consideration the fact that certain PEC elements will be hindered by the more significant differences (namely, a smaller double layer capacitance, higher high-frequency charge transfer resistance, and higher leakage current). Between these, the positive impact of the temperature increase far outpaces the negative impact to these elements. Double layer capacitance, for example (Equation 2.3 and 2.4), theoretically only drops around 40  $\mu\text{F}$  over a temperature change of 100. One must find the balance between how much the pyroelectric material can provide and how much the rest of the cell can store within the bounds of a specified temperature

difference without the real-world materials breaking down due to excessive heat.

## CHAPTER 6

### CONCLUSION

This work proposed and developed an equivalent circuit model for the PEC, integrating a modified Randle's circuit and a current source to model the pyroelectric energy harvesting mechanism. The model successfully emulates the open-circuit potential response of a PEC subjected to thermal cycling, aligning well with experimental data and providing valuable insight into the interplay between energy harvesting and storage processes within the device. By leveraging circuit-based modeling, this research establishes a foundation for optimizing PEC designs and exploring its potential as a sustainable energy harvesting technology.

Findings from this study highlight the critical impact of material selection on PEC performance. Specifically, pyroelectric coefficient ( $p$ ), electrolyte conductivity ( $\sigma$ ), and separator permittivity ( $\epsilon_s$ ) were found to be key parameters influencing energy density. Maximizing  $p$  and  $\sigma$  while minimizing  $\epsilon_s$  enhances energy harvesting efficiency by increasing the strength of the internal electric field and improving ion transport within the electrolyte. Other parameters, such as separator thickness ( $L_s$ ) and porosity ( $\gamma_s$ ), demonstrated secondary influence on area-based energy density, suggesting that moderate variations in these values do not significantly affect performance. Additionally, achieving high leakage resistance ( $R_2$ ) is crucial for maintaining a sufficiently long relaxation time constant ( $\tau_2$ ), particularly in applications with extended thermal cycles.

Despite the model's successes, it carries certain limitations that warrant further investigation. One primary limitation is the use of a fitting factor ( $k$ ) in the pyroelectric field equation (Equation 2.10), which is currently treated as an empirical parameter rather than derived from first principles. This restricts the model's predictive accuracy, as the physical dependence of  $k$  on separator properties—such as pore structure, tortuosity, and dielectric behavior—remains unclear. Future research should focus on refining the characterization

of  $k$  by establishing a theoretical framework that links it directly to measurable physical properties of the separator. Doing so would enhance the model's ability to predict PEC behavior under a wider range of conditions without relying on empirical adjustments.

The incorporation of energy density calculations alongside cell characterization simulations (EIS, CV, amperometry, and OCP) provides a comprehensive means of linking the PEC's energy harvesting and storage capabilities. Our approach allows for a quantitative assessment of performance across different design configurations, offering a clearer pathway for targeted improvements. Future work should expand upon these results by performing a multi-variable optimization of the PEC, considering both material properties and operational conditions to maximize energy output.

Ultimately, this research represents a step forward in the development of PECs as a viable technology for sustainable energy harvesting. Continued advancements in modeling and experimental validation will enable more precise control over device performance, facilitating the transition from prototype to practical implementation. By addressing current limitations and refining the predictive power of the equivalent circuit model, future studies can help unlock the full potential of PECs for real-world low-power applications, particularly in autonomous IoT devices that require reliable, off-grid energy sources.

## APPENDIX A

### SUPPLEMENTARY INFORMATION

#### Effect of Starting OCP

Equivalent circuit model OCP simulations used in this work are all based on a starting cell OCP of 0 mV. The effect of starting OCP on  $\Delta$ OCP for a thermal cycle is shown in Figure S1 for two different values of  $R_2$ . Low-frequency branch resistance has been attributed to EDLC leakage current and charge redistribution effects. In Figure S1a, a “low”  $R_2$  value of 950  $\Omega$  prevents the cell from achieving an OCP  $>$  1.5 mV at the end of a 20-30-20  $^{\circ}$ C thermal cycle. In Figure S1b, a “high”  $R_2$  value of 1 G $\Omega$  enables higher final values of OCP.

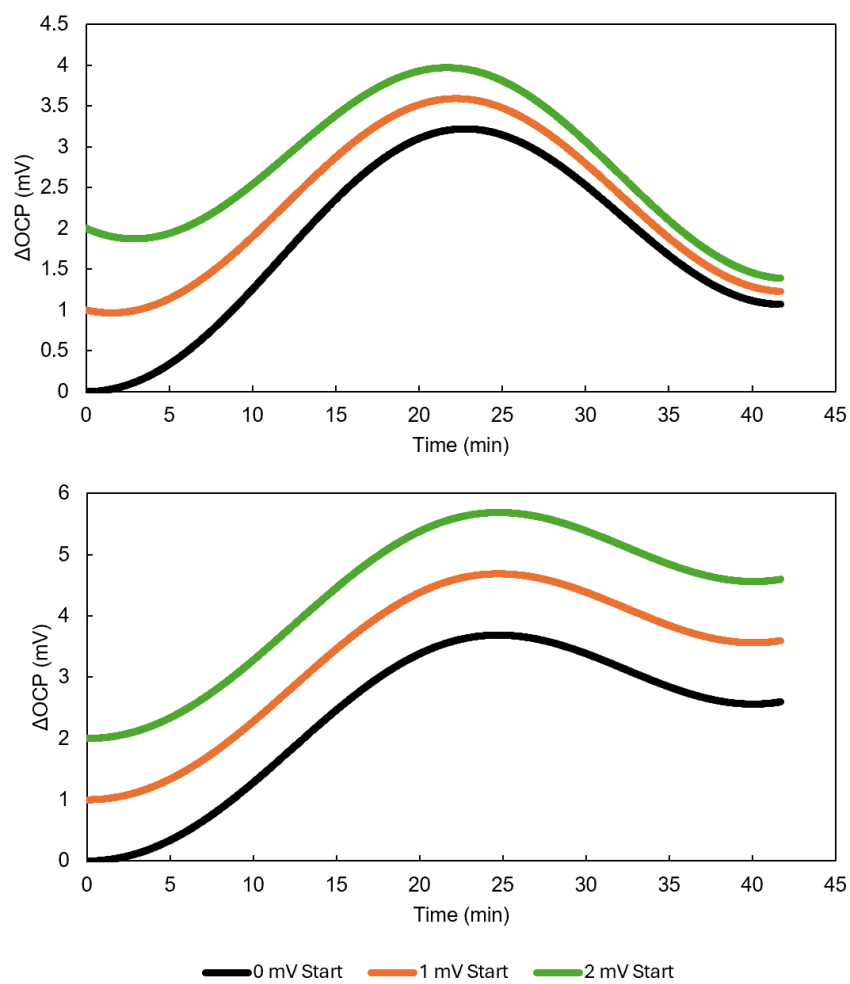


**Figure S1.** Effect of starting OCP on PEC thermal charging. Simulations were conducted with three values of starting OCP (0 mV, 1 mV, and 2 mV) with  $R_2 = 950 \Omega$  (a) and  $R_2 = 1 \text{ G}\Omega$  (b).

## Peak vs. Mid-Cycle $\Delta$ OCP

All  $\Delta$ OCP and  $U_A$  values reported in the manuscript are based on a full thermal cycle. These values could also be extracted at the cycle peak, before the temperature returns to its initial value. Extracting  $\Delta$ OCP at the peak vs. end of a thermal cycle will affect the magnitude of  $U_A$ , however we do not expect it to affect the outcomes of the model-based parameter exploration performed in section 5. Figure S2 provides  $\Delta$ OCP simulation results for a 20-30-20 °C thermal cycle with  $p = 59 \mu\text{C}/\text{m}^2\text{K}$  (“1x pyro coefficient”) and  $p = 118 \mu\text{C}/\text{m}^2\text{K}$  (“2x pyro coefficient”). The resulting scaling factor of  $\Delta$ OCP is seen to be approximately the same whether  $\Delta$ OCP is taken as the start-to-peak value or start-to-end value of the thermal cycle.

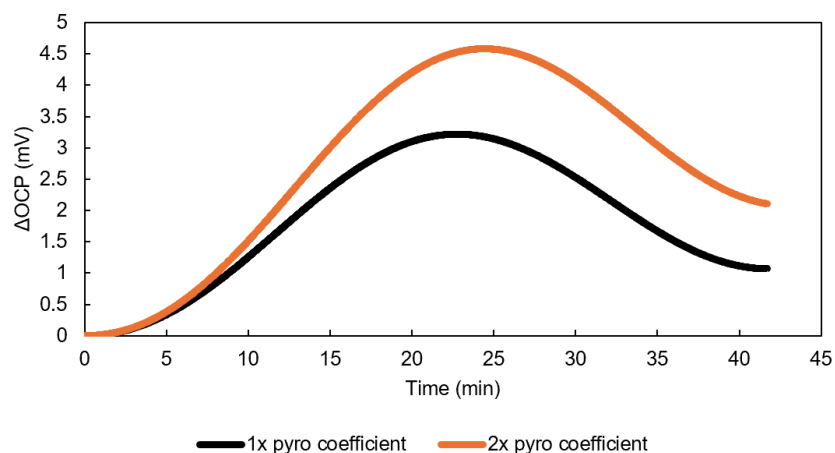


**Figure S2.** OCP simulation for one thermal cycle (20-30-20 °C) with  $p = 59 \mu\text{C}/\text{m}^2\text{K}$  (“1x pyro coefficient”) and  $p = 118 \mu\text{C}/\text{m}^2\text{K}$  (“2x pyro coefficient”).

## REFERENCES

- [1] S. AHANKARI, D. LASRADO, AND R. SUBRAMANIAM, *Advances in materials and fabrication of separators in supercapacitors*, Mater. Adv., 3 (2022), pp. 1472–1496.
- [2] D. ANDELMAN, *Chapter 12 - electrostatic properties of membranes: The poisson-boltzmann theory*, in Structure and Dynamics of Membranes, R. Lipowsky and E. Sackmann, eds., vol. 1 of Handbook of Biological Physics, North-Holland, 1995, pp. 603–642.
- [3] P. BENCIS AND M. ALKTRANEE, *The potential of vehicle cooling systems*, in Journal of physics: Conference series, vol. 1935, IOP Publishing, 2021, p. 012012.
- [4] T. BOUGUERA, J.-F. DIOURIS, J.-J. CHAILLOUT, R. JAOUADI, AND G. ANDRIEUX, *Energy consumption model for sensor nodes based on lora and lorawan*, Sensors, 18 (2018).
- [5] C. BOWEN, J. TAYLOR, E. LE BOULBAR, D. ZABEK, AND V. TOPOLOV, *A modified figure of merit for pyroelectric energy harvesting*, Materials Letters, 138 (2015), pp. 243–246.
- [6] C. R. BOWEN AND M. H. ARAFA, *Energy harvesting technologies for tire pressure monitoring systems*, Adv. Energy Mater., 5 (2015), p. 1401787.
- [7] C. R. BOWEN, J. TAYLOR, E. LEBOULBAR, D. ZABEK, A. CHAUHAN, AND R. VAISH, *Pyroelectric materials and devices for energy harvesting applications*, Energy Environ. Sci., 7 (2014), pp. 3836–3856.
- [8] C. BYOUNG-YONG, *Conversion of a constant phase element to an equivalent capacitor*, J. Electrochem. Sci. Technol, 11 (2020), pp. 318–321.
- [9] M. CANALES AND E. GUÀRDIA, *Computer simulation study of ion-water and water-water hydrogen bonds in sulfuric acid solutions at low temperatures*, Journal of Molecular Liquids, 347 (2022), p. 118351.
- [10] B.-Y. CHANG, *The effective capacitance of a constant phase element with resistors in series*, Journal of Electrochemical Science and Technology, 13 (2022), pp. 479–485.
- [11] A. CUADRAS, M. GASULLA, AND V. FERRARI, *Thermal energy harvesting through pyroelectricity*, Sensors and Actuators A: Physical, 158 (2010), pp. 132–139.
- [12] H. ELAHI, K. MUNIR, M. EUGENI, S. ATEK, AND P. GAUDENZI, *Energy harvesting towards self-powered iot devices*, Energies, 13 (2020).
- [13] W. GANNON AND C. DUNNILL, *Apparent disagreement between cyclic voltammetry and electrochemical impedance spectroscopy explained by time-domain simulation of constant phase elements*, International Journal of Hydrogen Energy, 45 (2020).
- [14] S. M. GATEMAN, O. GHARBI, H. GOMES DE MELO, K. NGO, M. TURMINE, AND V. VIVIER, *On the use of a constant phase element (cpe) in electrochemistry*, Current Opinion in Electrochemistry, 36 (2022), p. 101133.

- [15] W. GUO, C. YU, S. LI, AND J. QIU, *Toward commercial-level mass-loading electrodes for supercapacitors: opportunities, challenges and perspectives*, *Energy Environ. Sci.*, 14 (2021), pp. 576–601.
- [16] R. HASTAK, P. SIVARAMAN, D. POTPHODE, K. SHASHIDHARA, AND A. SAMUI, *All solid supercapacitor based on activated carbon and poly [2,5-benzimidazole] for high temperature application*, *Electrochimica Acta*, 59 (2012), pp. 296–303.
- [17] B. HIRSCHORN, M. E. ORAZEM, B. TRIBOLLET, V. VIVIER, I. FRATEUR, AND M. MUSIANI, *Determination of effective capacitance and film thickness from constant-phase-element parameters*, *Electrochimica Acta*, 55 (2010), pp. 6218–6227. IMPEDANCE SPECTROSCOPY AND TRANSFER FUNCTIONS.
- [18] Q. JU AND Y. ZHANG, *Reducing charge redistribution loss for supercapacitor-operated energy harvesting wireless sensor nodes*, in *Proceedings of the 2nd International Workshop on Energy Neutral Sensing Systems, ENSsys '14*, New York, NY, USA, 2014, Association for Computing Machinery, p. 31–36.
- [19] J. KANG, S. H. JAYARAM, J. RAWLINS, AND J. WEN, *Characterization of thermal behaviors of electrochemical double layer capacitors (edlcs) with aqueous and organic electrolytes*, *Electrochimica Acta*, 144 (2014), pp. 200–210.
- [20] V. KESLER, B. MURMANN, AND H. T. SOH, *Going beyond the debye length: Overcoming charge screening limitations in next-generation bioelectronic sensors*, *ACS Nano*, 14 (2020), pp. 16194–16201. PMID: 33226776.
- [21] T. KOWALCHIK, F. KHAN, D. HORLACHER, S. ROUNDY, AND R. WARREN, *Direct conversion of thermal energy to stored electrochemical energy via a self-charging pyroelectrochemical cell*, *Energy Environ. Sci.*, 17 (2024), pp. 2117–2128.
- [22] J. LANDESFEIND, J. HATTENDORFF, A. EHRL, W. A. WALL, AND H. A. GASTEIGER, *Tortuosity determination of battery electrodes and separators by impedance spectroscopy*, *Journal of The Electrochemical Society*, 163 (2016), p. A1373.
- [23] K. LIU, C. YU, W. GUO, L. NI, J. YU, Y. XIE, Z. WANG, Y. REN, AND J. QIU, *Recent research advances of self-discharge in supercapacitors: Mechanisms and suppressing strategies*, *Journal of Energy Chemistry*, 58 (2021), p. 94–109.
- [24] Z. LIU, Y. JIANG, Q. HU, S. GUO, L. YU, Q. LI, Q. LIU, AND X. HU, *Safer lithium-ion batteries from the separator aspect: Development and future perspectives*, *ENERGY & ENVIRONMENTAL MATERIALS*, 4 (2021), pp. 336–362.
- [25] C. MASARAPU, H. F. ZENG, K. H. HUNG, AND B. WEI, *Effect of temperature on the capacitance of carbon nanotube supercapacitors*, *ACS Nano*, 3 (2009), pp. 2199–2206. PMID: 19583250.
- [26] A. A. MIRGHNI, M. J. MADITO, T. M. MASIKHWA, K. O. OYEDOTUN, A. BELLO, AND N. MANYALA, *Hydrothermal synthesis of manganese phosphate/graphene foam composite for electrochemical supercapacitor applications*, *Journal of Colloid and Interface Science*, 494 (2017), pp. 325–337.

- [27] W. PELLETIER, K. V. CHAU, R. A. BUCKLIN, J. K. BRECHT, D. W. HAHN, AND J.-P. ÉMOND, *Analysis of air cargo temperature variations during transport operations*, Transactions of the ASABE, 61 (2018), pp. 723–732.
- [28] S. SADOWSKI AND P. SPACHOS, *Wireless technologies for smart agricultural monitoring using internet of things devices with energy harvesting capabilities*, Computers and Electronics in Agriculture, 172 (2020), p. 105338.
- [29] T. SANISLAV, G. D. MOIS, S. ZEADALLY, AND S. C. FOLEA, *Energy harvesting techniques for internet of things (iot)*, IEEE Access, 9 (2021), pp. 39530–39549.
- [30] O. A. SARAEREH, A. ALSARAIRA, I. KHAN, AND B. J. CHOI, *A hybrid energy harvesting design for on-body internet-of-things (iot) networks*, Sensors, 20 (2020).
- [31] S. SATHYAMOORTHY, V. SURYANARAYANAN, AND D. VELAYUTHAM, *Organo-redox shuttle promoted protic ionic liquid electrolyte for supercapacitor*, Journal of Power Sources, 274 (2015), pp. 1135–1139.
- [32] G. SEBALD, E. LEFEUVRE, AND D. GUYOMAR, *Pyroelectric energy conversion: Optimization principles*, IEEE Transactions on Ultrasonics, Ferroelectrics and Frequency Control, 55 (2008), p. 538–551.
- [33] M. SHI, Z. ZHANG, M. ZHAO, X. LU, AND Z. L. WANG, *Reducing the self-discharge rate of supercapacitors by suppressing electron transfer in the electric double layer*, Journal of The Electrochemical Society, 168 (2021), p. 120548.
- [34] E. STOLLER AND L. WAX, *Temperature variations in the surface layers of an agricultural soil*, Weed Research, 13 (1973), pp. 273–282.
- [35] S. SUBRAMANIAN, M. A. JOHNY, M. MALAMAL NEELANCHERY, AND S. ANSARI, *Self-discharge and voltage recovery in graphene supercapacitors*, IEEE Transactions on Power Electronics, 33 (2018), pp. 10410–10418.
- [36] V. I. VOLKOV, A. V. CHERNYAK, O. I. GNEZDILOV, AND V. D. SKIRDA, *Hydration, self-diffusion and ionic conductivity of  $Li^+$ ,  $Na^+$  and  $CS^+$  cations in nafion membrane studied by nmr*, Solid State Ionics, 364 (2021), p. 115627.
- [37] H. WANG AND L. PILON, *Intrinsic limitations of impedance measurements in determining electric double layer capacitances*, Electrochimica Acta, 63 (2012), pp. 55–63.
- [38] J. WU, N. QIN, B. YUAN, E. LIN, AND D. BAO, *Enhanced pyroelectric catalysis of  $BiVO_4$  nanowires for utilizing waste heat in pollution treatment*, ACS Applied Materials & Interfaces, 10 (2018), pp. 37963–37973.
- [39] W. WU, S. SHANBHAG, J. CHANG, A. RUTT, AND J. WHITACRE, *Relating electrolyte concentration to performance and stability for  $Ni_2(P_2O_7)_3/Na_0.44MnO_2$  aqueous sodium-ion batteries*, Journal of the Electrochemical Society, 162 (2015), pp. A803–A808.
- [40] S. ZEADALLY, F. K. SHAIKH, A. TALPUR, AND Q. Z. SHENG, *Design architectures for energy harvesting in the internet of things*, Renewable and Sustainable Energy Reviews, 128 (2020), p. 109901.

- [41] F. ZHANG, Y. ZHANG, J. SILVER, Y. SHAKHSHEER, M. NAGARAJU, A. KLINEFELTER, J. PANDEY, J. BOLEY, E. CARLSON, A. SHRIVASTAVA, B. OTIS, AND B. CALHOUN, *A batteryless 19w mics/ism-band energy harvesting body area sensor node soc*, in 2012 IEEE International Solid-State Circuits Conference, 2012, pp. 298–300.
- [42] L. ZHI, W. ZHANG, L. DANG, J. SUN, F. SHI, H. XU, Z. LIU, AND Z. LEI, *Holey nickel-cobalt layered double hydroxide thin sheets with ultrahigh areal capacitance*, *Journal of Power Sources*, 387 (2018), pp. 108–116.